Materials & Design 254 (2025) 114024

Contents lists available at ScienceDirect

Materials & Design

journal homepage: www.elsevier.com/locate/matdes

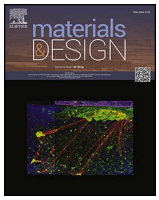

Experimental investigation via torsion testing and simulation of static recrystallization of ferrite in ultra-low carbon steel

Markus Führer [a,c,*], Philipp Retzl [c], Robert Kahlenberg [c,d], Sabine Zamberger [b], Phillip Haslberger [b], Ernst Kozeschnik [c], Erwin Povoden-Karadeniz [a,c]

[a] Christian Doppler Laboratory for Interfaces and Precipitation Engineering CDL-IPE, Institute of Materials Science and Technology, TU Wien, Getreidemarkt 9, 1060 Vienna, Austria
[b] Voestalpine Forschungsservicegesellschaft Donawitz GmbH, Kerpelystraße 199, 8700 Leoben, Austria
[c] Institute of Materials Science and Technology, TU Wien, Getreidemarkt 9, 1060 Vienna, Austria
[d] Materials Center, Leoben Forschung GmbH, Roseggerstraße 12, Leoben 8700, Austria

ARTICLE INFO

Keywords:
Computational materials engineering
Ultra-low carbon steel
Static recrystallization
Cold torsion test
Microstructure control

ABSTRACT

High-strain cold deformation introduces high driving forces for recrystallization, i.e., high dislocation densities, which in turn remarkably alters the microstructure. The static recrystallization behavior of ultra-low carbon steel during annealing, following cold torsion tests with engineering strain greater than 2, is experimentally investigated. Metallographic and EBSD analysis are used to evaluate the resulting microstructure after deformation and annealing. The recrystallized grain size decreases with increasing strain until reaching a saturation point. The study reveals that torsion tests are well suited to investigate the recrystallization behavior for a wide range of strain in ferritic steel. The experimental results are compared to computer simulations using a mean-field recrystallization model implemented in MatCalc. By using an extended Kocks-Mecking model approach and considering the subgrain boundary misorientation, the simulations consistently reproduce the experimental results, validating the accuracy of the model.

1. Introduction

Metal forming techniques that are carried out at room temperature, such as thread rolling or deep drawing, can induce high local strains ($\varepsilon > 2$) [1], leading to remarkably high dislocation densities. The associated high stored deformation energy is the driving force for the competing mechanisms of recrystallization and recovery, thus strongly influencing the microstructure evolution [2], which makes their control and predictability industrially relevant. Primary static recrystallization (SRX) during annealing after plastic deformation changes the grain shape and the crystallographic texture. The form of grains changes from elongated and heavily deformed grains to small, equiaxed grains, thus decreasing the average grain size, which is a significant strengthening mechanism in steel generally and also in ferritic, body-centered cubic (BCC) steel [3]. The resulting recrystallized grain size decreases to some extent with increasing deformation but is hardly influenced by the annealing temperature if no grain growth occurs [2,4,5]. Moreover, the recrystallization behavior is connected to the crystallographic orientation, which can be controlled to some extent by the degree of plastic deformation and the mobility of grain boundaries [4], which is influenced by grain boundary pinning due to second-phase particles and solute drag [4]. In particular, it has been shown that segregated manganese atoms at grain boundaries lower the mobility of grain boundaries and thus slow down the ferrite growth kinetics [6,7].

Many groups have given special emphasis, e.g., [2,8–11], to the SRX behavior of hypo-eutectoid steel in the austenitic region. In contrast, existing studies on the SRX behavior of ferrite in low-carbon steel mainly deal with compression tests and strains up to 80 %. By investigating deformed material with engineering strain greater than two after torsion testing, we want to address this gap. Diehl et al. [4] examine the nucleation and recrystallization process of a commercial unalloyed low-carbon steel using electron backscatter diffraction (EBSD) after a rolling reduction of 65 %. They investigate the recrystallized microstructure and observe the nucleation of new grains, especially in highly deformed regions, with the newly nucleated grains inheriting the orientation from the deformed microstructure. Ogawa et al. [12] examine the behavior of cold-rolled low-carbon steel during intercritical annealing after a reduction of 67 % and find a retardation of ferrite recrystallization and a

* Corresponding author.
E-mail address: markus.fuehrer@tuwien.ac.at (M. Führer).

https://doi.org/10.1016/j.matdes.2025.114024
Received 23 December 2024; Received in revised form 25 April 2025; Accepted 29 April 2025
Available online 1 May 2025

strain induced formation of austenite at the interface between recrystallized and non-recrystallized ferrite grains. Herrera et al. [13] and Tavakoli et al. [14,15] investigate the influence of cold rolling and subsequent annealing at temperatures ranging from 500 °C to 720 °C for medium carbon steel and a rolling reduction between 35 % and 90 %. The latter report provides valuable insight into the SRX kinetics, incorporating the effects of annealing temperature and reduction in thickness. Chbihi et al. [16] and Alaneme [17] study the competition between ferrite recrystallization and austenite formation in medium carbon low alloy steel and find a strong interdependence between ferrite recrystallization and austenite formation.

In terms of analyzing the resulting microstructure after torsional deformation and annealing, Whitley et al. [18], Wright et al. [19], and Diehl et al. [4] made relevant contributions. Whitley et al. [18] investigated the resulting strain after thermomechanical torsional deformation of steel in the austenite region by microstructural observation. Wright et al. [19] and Diehl et al. [4] contributed by providing methods for investigating the recrystallized areas via EBSD. Considering an approach by Pantleon [20] on resolving geometrically necessary dislocations (GNDs) by EBSD provides a lower limit for the total dislocation density that can be approximated by using the crystal orientation from EBSD measurements.

Since the excess dislocation density is the driving force for SRX, correct consideration of dislocations in crystalline material is crucial. Nye [21] and Ashby [22] divide dislocations into GNDs and statistically-stored dislocations (SSDs) [23]. The former type (GNDs) appears per definition in strain gradient fields dependent on the geometrical constraints of the crystal lattice. The latter type (SSDs) arises from random trapping during plastic deformation [22,23]. Breitbarth et al. [24] state that in Aluminum at low strain (< 2 %), SSD-density measured with electron channeling contrast imaging (ECCI) is 10 times higher than GND-density measured with EBSD. Zhu et al. [25] investigate the evolution of SSDs and GNDs up to a strain of 0.46 by measuring the latter with EBSD. The authors calculate the SSD-density by subtracting the GND-density from the estimated total dislocation density according to Taylor's hardening model [26]. Zhu et al. find that only at very low strain the GND-density is bigger than the SSD-density, i.e., 0.09 for a grain size of 30 μm in Nickel.

For describing recrystallization kinetics at constant temperature, the Johnson-Mehl-Avrami-Kolmogorov equation (JMAK) is often used [15,27,28]. With this analytical equation, the volume fraction of the recrystallized grains, dependent on two parameters, can be calculated. Rios and Villa [28] show that the spatially varying dislocation density widely influences the recrystallization behavior and that assuming a constant growth velocity of the new phase is unjustified for good spatial resolution [4]. Medina and Quispe [29] model the recrystallization plateaus with two interrelated transformation curves using an empirical Avrami approach [30] and considering the influence of solute drag with different activation energies. Rehman and Zurob [31] present an approach where the recrystallization plateaus are taken into account by pinned dislocations. For the impact of solute drag, the approach by Cahn [32] is used. Bailey and Hirsch [33] provide a model for static recrystallization, where subgrains in contact with high-angle grain boundaries can act as newly recrystallized grains and continue growing into the adjacent grain. In this model, the driving force for recrystallization results from the stored deformation energy, which is directly related to the total dislocation density. Gil Sevillano et al. [34] and Kaibyshev et al. [35] mention the increase of subgrain boundary misorientation with strain. The subgrain boundary misorientation, dependent on the total strain, influences the recrystallization behavior via the number of GNDs to maintain given substructure characteristics, e.g., subgrain size [36]. Therefore, the evolution of subgrain boundary misorientation versus strain is crucial for accurately describing the total dislocation density evolution and, consequently, the amount of stored deformation energy.

The present work contributes to understanding the SRX behavior of cold-deformed, ultra-low carbon steel up to high strains of 2 via experimental torsion testing and annealing combined with computational simulations using the software package MatCalc [37]. The novelty of this work lies in the combination of different models for correctly describing the resulting fraction of recrystallized grains and the resulting grain size. In the simulative part, we integrate models for substructure evolution by Kocks-Mecking [38] and for static recrystallization by Bailey-Hirsch, as introduced by Buken et al. [39]. This model uses the total excess dislocation density as the driving force for static recrystallization. Furthermore, we have developed a description for the subgrain misorientation angle evolution, which is crucial for understanding the substructure evolution and the evolution of the dislocation density during stage IV hardening.

On the experimental side, torsion tests for ultra-low carbon steel with engineering strain greater than 2 in the ferrite temperature region are performed. The advantages of torsion tests are higher strain and a wide strain variation compared to rolling [40] and compression tests often used for similar experimental investigations. We show that microstructural observations of steel after cold-torsional deformation can reasonably accurately quantify the resulting strain in ferrite. The torsional deformation and the subsequent annealing at different temperatures ranging from 500 °C to 700 °C for 120 s are carried out on a Gleeble [41] thermomechanical simulator. The results are analyzed in the tangential longitudinal plane at the effective radius, which is given by 0.724 times the radius (R), referred to as the tangential plane of interest, and in the specimen cross-section. We experimentally investigate the evolution of grain size and recrystallized fraction based on strain and annealing temperature by optical light microscopy (LOM) and EBSD. The resulting strain after deformation in the tangential plane of interest is controlled by adapting the methodology of Whitley et al. [18] for ferrite, where the inclination angle between non-recrystallizing particles, like manganese-sulfide (MnS) and the axis of symmetry can be used for determining the resulting strain. Additionally, we employ EBSD to analyze the resulting state of the microstructure and evaluate the recrystallized fraction and the resulting ferrite grain size. The objective of this study is to elaborate a precise methodology capable of forecasting the kinetic parameters associated with recrystallization and the progression of grain size during the process of static recrystallization in ferrite in ultra-low carbon steel, both of which are contingent upon the magnitude of applied strain.

2. Materials and methods

2.1. Material

An ultra-low carbon steel with the chemical composition shown in Table 1 is used to examine the static recrystallization mechanism. We choose this material to minimize the influence of grain boundary pinning (Zener pinning [42]) by carbonitride precipitates or solute drag [32] by different microalloying elements such as Nb or Ti. The initial microstructure is ferrite with a grain size of 33 μm.

2.2. Torsion tests

2.2.1. Experimental setup

The time–temperature-deformation history in Fig. 1 consists of a torsional deformation at room temperature on a Gleeble 3800 [41] thermo-mechanical simulator with a total torsional angle of 13.4 rad. For further detail on torsion testing, it is referred to [43,44]. A heat treatment with different soaking temperatures held for 120 s and a subsequent quenching step to freeze the microstructure is applied to investigate the static recrystallization behavior and the associated ferrite grain evolution.

Table 2 summarizes the variations in soaking temperature and strain rate. The comparison of a low strain rate of 0.1 s^{-1} with a high strain rate of 10 s^{-1} at 700 °C provides insight into the influence of the deformation speed on the microstructure evolution.

Fig. 2 shows the cylindrical specimen's geometry, with the gauge

Table 1
Chemical composition of the examined steel in wt.%.

C	Al	N	Mn	S	Cr	Cu	Si	Nb	Ti	Fe
0.02	0.05	0.003	0.2	0.009	0.02	0.02	0.0064	0.001	0.001	bal.

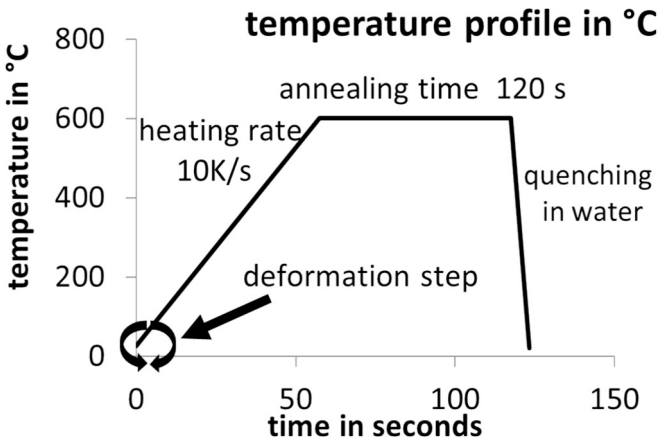

Fig. 1. Time-temperature-deformation profile.

Table 2
List of carried-out experiments with corresponding strain rate and soaking temperature.

Experiment Nr.	Strain rate [1/s] $\dot{\phi}$	Soaking temperature [°C] T_s
1	0.1	700
2	10	500
3	10	600
4	10	700

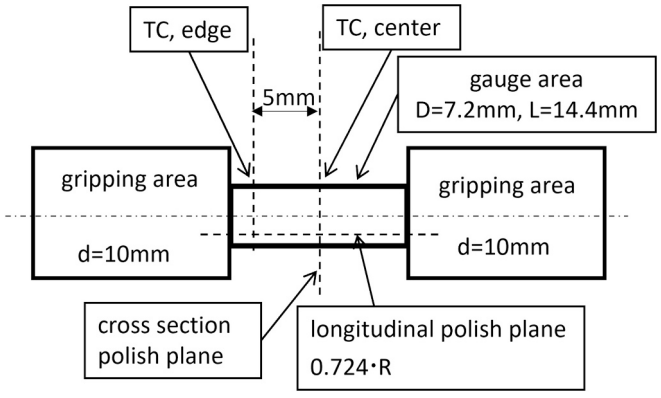

Fig. 2. Sample geometry, positions of the thermocouples (TC) on the sample, positions of the polish planes (cross-section and longitudinal).

area dimensions being 7.2 mm in diameter and 14.4 mm in length. The gripping area, with a diameter of 10 mm, is assumed to be free of deformation, resulting in strain occurrence only in the gauge area. With one thermocouple type K placed in the center for temperature control of the experiment and another placed 5 mm from the center for temperature measurement, the resulting temperature at the surface is monitored. The assumption of constant temperature over the whole radius is legitimate because of the small dimensions of the sample. For the subsequent microstructure investigation, we cut the specimen precisely at the longitudinal and cross-section plane. The longitudinal polish plane (Fig. 2) provides insight into the resulting strain, following the approach by Whitley et al. [18]; see Section 2.3. The cross-section polish plane provides a strain variation across the radius, which makes it possible to investigate the influence of the shear strain on the resulting microstructure.

2.2.2. Evaluation of stress–strain evolution from torsion tests

The driving force for recrystallization increases with increasing strain, which evolves with altering the radius position in the cross-section of the cylindric specimen. Torque T and twist ϑ are obtained from the torsion test on the Gleeble and provide the basis for the calculation of the shear strain $\varepsilon_{\text{shear}}$, effective strain ε_{eff}, and effective stress σ_{eff}. The local values of the shear strain across the radius (R), length of the gauge area (L), according to Gräber and Pöhlandt [45], are obtained from Eq. (1).

$$\varepsilon_{\text{shear}} = \frac{\vartheta \cdot R}{L} \tag{1}$$

According to the von Mises criterion, adapted by Maccagno et al. [46] and Medina et al. [11], the value for ε_{eff} is given by Eq. (2),

$$\varepsilon_{\text{eff}} = \frac{\vartheta \cdot R}{\sqrt{3}L} \tag{2}$$

2.3. Evaluation of shear strain from microstructural observations

We use a method developed by Whitley et al. [18] to evaluate the accumulated shear strain after the deformation step. This approach measures the inclination angle θ' between inclusions, such as manganese sulfide MnS, and the reference line at the effective radius R_{eff} in the longitudinal polish plane. The reference line is parallel to the torsional axis with a distance of $R_{\text{eff}} = 72.4$ % of the gauge radius, as developed by Barraclough et al. [47]. The advantage of this position is the minimization of the effects of strain rate sensitivity and strain hardening behavior [47], i.e., the smallest affection on the values of stress and strain [18]. Evaluating the microstructure at a certain distance from the surface avoids the influence of, for instance, oxidation or decarburization on the microstructure [5].

Fig. 3 shows the expected morphological features after torsional deformation in ferrite and the position of each feature with respect to the reference line, according to Whitley et al. [18]. Features A and B, representing inclusions such as MnS and non-recrystallized ferrite grains, respectively, are expected to reflect the impact of the locally accumulated shear strain, analogously to the approach by Whitley et al. [18] for torsional deformation in austenite and can therefore be used to determine the inclination angle. Feature C symbolizes recrystallized grains, which cannot be used to evaluate the imposed shear strain. We imply that (i) before deformation, ferrite grains are equiaxed, (ii) recrystallized grains grow isotropically in an equiaxed morphology [13,36], and (iii) during deformation, the cross-sectional area of each grain remains constant [18].

Fig. 4 shows the θ' as described in Fig. 3 to evaluate the accumulated shear strain in a tangential plane at radius position R_{eff} after torsional deformation and heat treatment. The specimens are either directly investigated under an optical microscope or etched with Nital etching agent to measure the inclination angle with MnS or with non-recrystallized ferrite grains, respectively. The samples are positioned under the microscope so that the lower horizontal edge of the image section coincides with the reference line. The angle between inclusions or non-recrystallized grains and the horizontal line depicts the inclination angle.

Eq. (3) gives the correlation between the inclination angle θ' and the

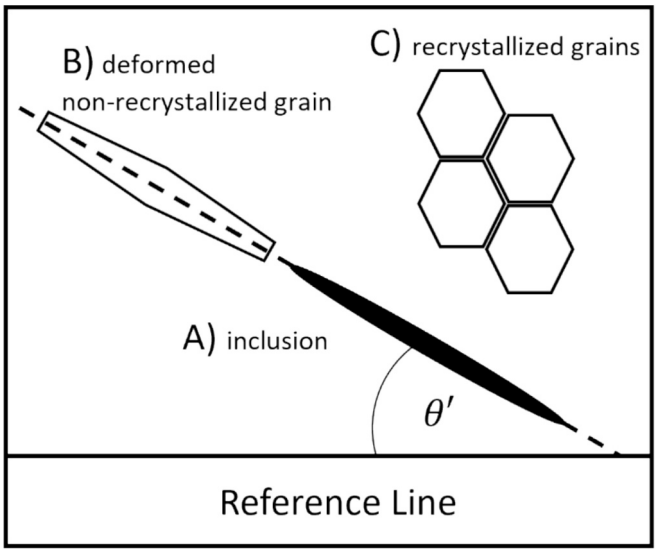

Fig. 3. Schematic representation of features in the ferritic microstructure after torsion testing and heat treatment. Adapted from Whitley et al. [18]. Inclusions, such as MnS (A), non-recrystallized ferrite grains (B), and recrystallized grains (C). The inclination angle θ‘ lies between the reference line and the features A and B.

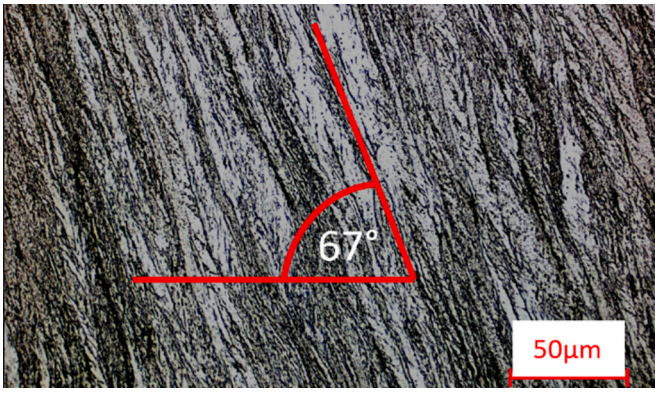

Fig. 4. Optical microscope image showing the inclination angle θ' between the reference line and non-recrystallized ferrite grains.

accumulated shear strain γ_{acc}.

$$\gamma_{acc} = \tan(\theta') \tag{3}$$

This correlation is confirmed by Whitley et al. [18] for austenite, which we analogously claim to be also valid for ferrite.

Note that ε and γ are used to describe strain after evaluation via Eqs. (1–2) or Eq. (3), respectively.

2.4. Electron backscatter diffraction analysis

The EBSD analysis delivers the crystal orientation and thus provides detailed information on the resulting microstructure, e.g., grain size and strain. The grain size can be evaluated via crystal orientation data by dividing the specimen into regions with similar orientations; high-angle grain boundaries (HAGBs) typically show misorientations bigger than 15° [48]. We analyze the cross-section plane of the samples with EBSD. For the sample preparation, we follow the recommended polishing routine for EBSD from Struers [49]. For the analysis of the EBSD data, we use the open-source MTEX toolbox [50]. With the crystal orientation data, the Kernel-Average-Misorientation (KAM) of directly connected neighbors (1st order) is evaluated for each point. In mapping the result, each value is assigned a particular color, from white (low KAM value) to dark red (high KAM value). It can reasonably be assumed that areas with a low KAM value (white areas) and a low local misorientation within the grains are recrystallized [23] since no deformation gradient is expected within a freshly recrystallized grain.

2.4.1. Grain size and recrystallized fraction

The grain size of differently strained material is evaluated with the line-cutting method [51] after etching with Nital, using a magnification of 500x in the light optical microscope. The line-cutting method is known to provide accurate results [51]. For each measured point, the standard error of the mean is calculated by taking a minimum of five measuring lines using the line-cutting method. To assess the recrystallized fraction in the cross-section in dependence of strain, we use LOM and EBSD in a field emission gun electron microscope (ZEISS Sigma 500) with EBSD attachment OIM of EDAX/TSL. All observations are made at 15 kV acceleration voltage, at a working distance of 14 mm, and with a step size of 0.1 µm.

2.4.2. Dislocations

We use the data from EBSD measurement and apply an approach by Pantleon [20] to estimate the GND-density. In this approach, local orientation measurements on planar surfaces allow for the determination of the dislocation density tensor, and finally, via linear optimization, a lower dislocation density bound is obtained. Statistically stored dislocations (SSDs), which also affect the total dislocation density and stored energy, can not be resolved by EBSD misorientation measurements and are thus not evaluated by this approach. Following the work by Zhu et al. [25] and Breitbarth et al. [24] on the evolution of GNDs and SSDs, we assume SSDs to be the dominant type, especially for high deformation levels.

3. Modeling

Recrystallization happens by the reconstructive movement of HABGs through a deformed microstructure, with the driving force for this process being the reduction of stored deformation energy. In the thermokinetic software package MatCalc (Version 6.05.0015) [37], the relevant mechanisms for describing static recrystallization, as described by Buken and Kozeschnik [52], are nucleation, growth, and coarsening of recrystallized grains, taking into account the dislocation density evolution and precipitation kinetics [53].

3.1. Substructure evolution model

The dislocation density evolution in MatCalc is based on an extended Kocks-Mecking model [54,55] as introduced by Sherstnev et al. [55]. It describes the dislocation density evolution with a single state parameter that is the total dislocation density ρ. The parameterization in Eq. (4) uses parameters A, B, and C, with the individual terms representing dislocation generation (A), dynamic recovery (B), and static recovery (C),

$$\frac{d\rho}{d\varphi} = \frac{M}{bA}\sqrt{\rho} - 2BM\frac{d_{crit}}{b}\rho - 2CD_{eff}\frac{Gb^3}{\dot{\varphi}kT}\left(\rho^2 - \rho_{req}^2\right), \tag{4}$$

with k being the Boltzmann constant, M the Taylor factor, b the Burgers vector, D_{eff} the effective diffusion coefficient [56], and $\dot{\varphi}$ the strain rate. d_{crit} in the dynamic recovery part (B) in Eq. (4) is the critical distance that two dislocations of opposite signs can be apart from each other and still have the possibility to spontaneously annihilate.

The required dislocation density to uphold a given substructure ρ_{req} [36] is the sum of the equilibrium dislocation density value ρ_{eq}, considered constant, and the wall dislocations ρ_b, Eq. (5).

$$\rho_{rep} = \rho_{eq} + \rho_b \tag{5}$$

The cell walls contain the geometrically necessary dislocations ρ_b to build up the given substructure, expressed by the Read-Shockley [57] geometrically necessary dislocations. Eq. (6) defines ρ_b via the subgrain diameter δ_{AV} and the subgrain boundary misorientation, Θ_{AV} with

$$\rho_b = \frac{\tan(\theta_{AV})}{b\delta_{AV}} \quad . \tag{6}$$

The subgrain size and the number of dislocations stored in cell walls are correlated through the principle of similitude [36], Eq. (7), which can be written in differential form as

$$\dot{\delta}_{AV} = \frac{\delta_{AV}^3}{2(A')^2} \, , \tag{7}$$

with the similitude parameter A' and the generation rate of excess mobile dislocations $\dot{\rho}_{ex}^{+}$. A decrease in subgrain size leads to an increase in stored energy density, which finally promotes recrystallization.

The evolution of the average sub-boundary misorientation Θ_{AV} depends on the material and the temperature [34,35,58–61]. For the experimental investigation of the subgrain – boundary misorientation variation with strain in aluminum, Schuh and von Heimendahl [62] use inter-dislocation spacing in sub-boundaries, and Nes [36] uses Kikuchi patterns from individual subgrains. Both conclude that the average subgrain – boundary misorientation increases rapidly to 3° at a strain of about 1, after which it remains constant to a strain of 4. Kaibyshev et al. [35] approximate the sub-boundary misorientation in a 1421 aluminum alloy within the strain range of 1 to 4 by the linear function $\theta_{AV} \approx 5^\circ \cdot \varepsilon_{eff}$. In our simulation, we opt for a cubic root [63] function to capture the actual behavior of Θ_{AV} at low strain instead of a linear description and to be more consistent with the recrystallization simulations, with $\theta_{AV} = 9 \cdot \sqrt[3]{\varepsilon_{eff}}$.

3.2. Static recrystallization model

In MatCalc, the static recrystallization model [39] is based on the Bailey-Hirsch mechanism [33], where subgrains that are in contact with HAGBs can nucleate as recrystallization seeds and subsequently grow into the adjacent grain when exceeding the critical subgrain diameter δ_{crit}^{RX}, given as

$$\delta_{crit}^{RX} = \frac{4\gamma_{HAGB}}{P_D^{RX}} = \frac{4\gamma_{HAGB}}{\frac{1}{2}Gb^2(\rho_D^{tot} - \rho_D^{equ})} \tag{8}$$

δ_{crit}^{RX} is influenced by the HAGB energy γ_{HAGB} and the driving pressure for recrystallization P_D^{RX}. P_D^{RX} is directly related to the total dislocation density (ρ_D^{tot}) i.e. the stored deformation energy. This model uses the HAGB energy (γ_{HAGB}) because a subgrain reaching critical size is treated as a new grain.

A Rayleigh distribution is used to approximate the distribution of subgrain sizes δ. The critical diameter evolves with time due to recovery and subgrain growth. It thus changes the fraction of subgrains that potentially develop into recrystallized nuclei over time. The evolution of the critical subgrain diameter (Eq. (8)) and the nucleation rate of recrystallized grains $\dot{N}$ are essential for SRX.

$$\dot{N} = N_{pot}^{RX} \cdot B^{RX} \cdot \dot{F}_1 \, . \tag{9}$$

$\dot{N}$ (Eq. (9)) depends on the number density of potential nucleation sites N_{pot}^{RX}, the saturation factor B^{RX} accounting for already recrystallized sites, and the flux of subgrains reaching the critical size $\dot{F}_1$.

3.3. Grain boundary pinning and solute drag

In the present model, the influence of solute elements and precipitates, which can retard the grain boundary movement, is accounted for by the solute drag mechanism using Cahn's model [32] and Zener pinning [42]. In MatCalc, these effects are taken into account simultaneously in the calculation of the mobility of HAGBs and low-angle grain boundaries (LAGB) [64]. The effective mobility M_{eff} is calculated taking the reciprocal sum of the intrinsic mobility without obstacles M_{int}, the mobility accounting for solute drag M_{sol}, and the grain boundary mobility in the presence of precipitates M_{prec}, Eq. (10).

$$\frac{1}{M_{eff}} = \frac{1}{M_{int}} + \frac{1}{M_{prec}} + \frac{1}{M_{sol}} \quad . \tag{11}$$

Values of 2500J/mol and 1500J/mol for the interaction energy with Manganese were reported by Zurob et al. [6] and Benrabah et al. [7], respectively. Benrabah et al. [7] explain this discrepancy with the differences in the thermodynamic models for interface mobility used by these two authors. For the mobility, the binding energy E_b of a substitutional element at the interface is a relevant property, which is, however, not known experimentally and is generally treated as a fitting parameter.

3.4. Grain growth – Movement of HAGBs

In MatCalc, the model implementation of grain growth has been described by Buken and Kozeschnik [39], with the change in grain diameter $\dot{D}$ being determined by the effective mobility M_{eff} and the driving pressure P_D^{tot}, as

$$\dot{D} = M_{eff} \cdot P_D^{tot} \, . \tag{11}$$

P_D^{tot}, consists of two parts, as seen in Eq. (12): The first part, P_D^{GG}, describes the tendency to minimize the total surface area. The associated growth and coarsening of grains is similar to the one under the effect of Laplace pressure [42]. The second part of P_D^{tot} denotes the driving force for recrystallization (P_D^{RX}) due to deformation, which is the driving pressure for the movement of HAGB in Eq. (8) [2],

$$P_D^{tot} = P_D^{GG} + P_D^{RX} = k_d \cdot \gamma_{HAGB}\left(\frac{1}{R_m} - \frac{1}{R}\right) + \frac{Gb^2}{2} \cdot (\rho_D^{tot} - \rho_D^{equ}) \, , \tag{12}$$

with k_d being the grain diameter evolution coefficient, R_m and R being the mean radius and the radius of the grain, respectively.

3.5. Incubation time

In Sections 3.1 to 3.4, we implicitly assume that we are dealing with a perfectly established substructure, which implies that supercritical subgrains/deformed regions around precipitates will immediately transform into recrystallized grains as soon as a critical value is reached. However, in reality, it can be expected that before the formation of a perfect recrystallized grain, some rearrangement of dislocations and HAGBs is necessary, for which thermal activation is required (at least in the static case). If this is not accounted for, recrystallization at room temperature after cold deformation is, in principle, a possible outcome of the simulation. To address this issue, an incubation distance is defined as the path that a HAGB traveled on average under the given driving forces due to deformation. In the case of Bailey-Hirsch nucleation [33], this mechanism sort of represents the bulging out of the HAGB where the new recrystallized grain has formed. The incubation factor f_{inc} is calculated with the bulging distance, d_{bulge}, and the critical subgrain diameter, δ_{crit}^{RX}, as

$$f_{inc} = 1 - \exp\left(-\frac{d_{bulge}}{\delta_{crit}^{RX}}\right) \tag{13}$$

f_{inc} multiplied with the nucleation rate $\dot{N}$, Eq. (9), provides a modulated amount of nucleating grains, considering incubation time. In essence, this approach prohibits the instantaneous nucleation of a new grain from

a supercritical subgrain up to a certain delay.

4. Simulation setup

Experimentally evaluated stress–strain curves of the used material give insight into the evolution of the dislocation density during plastic deformation via the Taylor Equation, as Eq. (14),

$$\sigma = \alpha M G b \sqrt{\rho} \tag{14}$$

which describes the relation between the true stress σ and the dislocation density ρ. α is the strengthening coefficient, depending on slip mode, dislocation arrangement, and dislocation density [65]. M, G, and b represent the Taylor factor, the shear modulus, and the Burgers vector, respectively. This expression, Eq. (14), allows for the derivation of the dislocation density evolution as a function of strain from a given stress–strain curve. Sobotka et al. [66] summarize the usage of stress–-strain curves and the parametrization of the dislocation density evolution model. We assume no static recovery at low temperatures. Thus, the parameter for static recovery (C) in the substructure evolution model is set to a very low value, $1 \cdot 10^{-9}$. Table 3 summarizes the input variables used for the thermokinetic simulation.

Table 3
Used parameters for the thermokinetic simulation in MatCalc.

Symbol	Name	Value	Unit	Source
α	Strengthening coeff.	0.25	–	This work
ν	Poisson's ratio	0.30	–	MatCalc def[a].
G	Shear modulus	$\frac{210000 - 75 \times T[C]}{2(1+\nu)}$	MPa	MatCalc def[a].
b	Burgers Vector	$2.5 \cdot 10^{-10}$	m	MatCalc def[a].
M	Taylor factor	2.5	–	MatCalc def[a].
k	Boltzmann constant	$1.381 \cdot 10^{-23}$	JK^{-1}	MatCalc def[a].
ρ_{eq}	equ. dislocation density	10^{12}	m^{-2}	MatCalc def[a].
D_G	Initial grain diameter	$33 \cdot 10^{-6}$	m	This work
D_{SG}	Initial subgrain diameter	$33 \cdot 10^{-6}$	m	This work
A	substr. evo. param.[b] A	40	–	This work
B	substr. evo. param.[b] B	4	–	This work
C	substr. evo. param.[b] C	$1 \cdot 10^{-9}$	–	This work
A'	similitude parameter	60	–	This work
θ_{AV}	subgrain misorientation	$9 \cdot \sqrt[3]{\varepsilon_{eff}}\#$	–	This work
$E_{B,Mn}$	Solute drag binding energy of Mn	1000	$Jmol^{-1}$	This work
D_{eff}	Diffusion ratio disl./ bulk (pipe – diffusion)	$0.003 \cdot \exp^{-\frac{130000}{RT}}$	$m^b s^{-1}$	[67]
D_{GB}	Diffusion ratio GB/bulk	$0.0035 \cdot \exp^{-\frac{150000}{RT}}$	$m^b s^{-1}$	[67]
k_d	GD evolution coeff.	1.5	–	MatCalc def[a].
γ_{HAGB}	HAGB-energy	0.5	Jm^{-2}	MatCalc def[a].
γ_{LAGB}	LAGB-energy	0.3	Jm^{-2}	MatCalc def[a].
ω	Grain boundary width	10^{-9}	m	[31]
$\eta_{HAGB,int}$	Free HAGB-prefactor	0.015	–	[64]
$\eta_{HAGB,int}$	Free LAGB-prefactor	10	–	MatCalc def[a].
$\eta_{HAGB,pin}$	Pinned HAGB-prefactor	0.001	–	[8]
$\eta_{HAGB,pin}$	Pinned LAGB-prefactor	0.001	–	[8]

[a] MatCalc def. …. Default values in the software package MatCalc.
[b] Substructure evolution parameter, as described in Section 3.1.

5. Experimental results and discussion

5.1. Microstructures

The deformed and annealed samples are analyzed metallographically in the longitudinal plane at the effective radius R_{eff} (0.724 · R) and in the center cross-section plane after etching with Nital. In the longitudinal plane at R_{eff}, measuring the resulting shear strain γ_{acc} (Eq. (3) [18]) and by this determining the local shear strain is possible, which guarantees trustful statements on the recrystallization behavior and grain size. Fig. 5 shows the resulting microstructure after torsional deformation of 13.4 rad in the tangential plane of interest without heat treating the sample.

Evaluating the accumulated shear strain γ_{acc}, Eq. (3), by measuring the θ' between the horizontal reference line and the morphological features in the ferrite in Fig. 5 gives a value of 2.4, which is in good agreement with the calculated value for the local shear strain by Eq. (1), i.e., 2.32. The lower horizontal edge coincides with the reference line, see Section 2.3.

The resulting microstructures after torsional deformation and subsequent heat treatments with different annealing temperatures and strain rates in the longitudinal plane at R_{eff} are shown in Fig. 6.

By comparing Figs. 5 and 6a, we conclude that no recrystallization occurs after annealing at 500 °C. In contrast, after annealing at T_S = 600 °C, the microstructure is fully recrystallized (Fig. 6b). The non-recrystallization temperature (T_{NR}) thus lies between 500 °C and 600 °C. We assume that no significant recovery occurs during the cold torsion test since the deformation-induced temperature at the surface reaches 240 °C at maximum [68]. This is attributed to the negligible mobility of dislocations at temperatures approaching room temperature [69]. Note that grain shapes and sizes at 700 °C seem independent of the strain rate (Fig. 6c and 6d). This behavior is attributed to the negligible mobility of dislocations in steel and, thus also, the insignificant recovery [68] at low temperatures and the accumulation of high defect densities, i.e., mainly dislocations and crystallographic textures, which are assumed in the grains [2], independent of the strain rate. With the dislocations providing the driving force for SRX upon subsequent annealing, we conclude that within the experimental limit, there is no relevant effect of the strain rate on SRX but only by the magnitude of the strain. However, the temperature dependence at constant straining can be seen by comparing Fig. 6b and 6d: Higher temperatures increase the mobility of grain boundaries, facilitating grain growth and recrystallization. Accordingly, an increasing grain size from 3 μm at 600 °C to 10 μm at

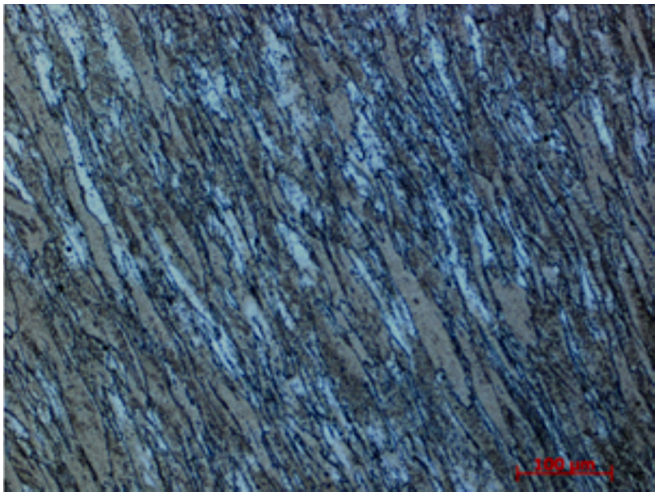

Fig. 5. Microstructure in the tangential plane of interest after torsional deformation with a torsional angle of 13.4 rad and without a subsequent annealing treatment; strain rate $\dot{\phi}$ = 10 s^{-1}, ε_{eff} = 1.34.

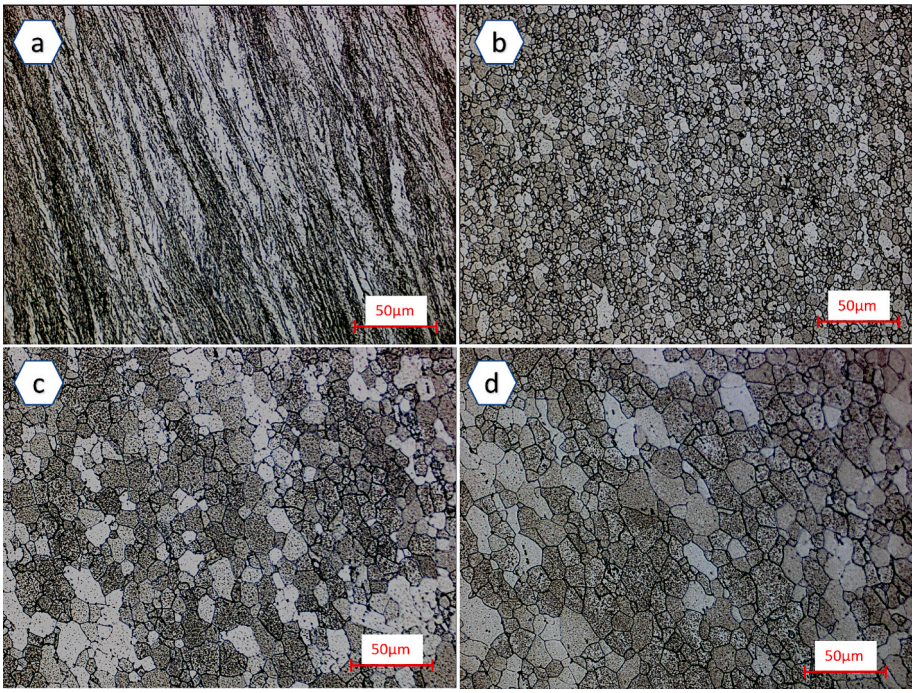

Fig. 6. Microstructure after torsion testing with a torsional angle of 13.4 rad and annealing treatment at different temperatures T_S and strain rates $\dot{\phi}$ at the effective radius (0.724·R, $\varepsilon_{eff} = 1.34$) in the longitudinal plane. a) $T_S = 500$ °C, strain rate$\dot{\phi} = 10\ s^{-1}$, b) $T_S = 600$ °C, $\dot{\phi} = 10\ s^{-1}$, c)$T_S = 700$ °C, $\dot{\phi} = 0.1\ s^{-1}$, d)$T_S = 700$ °C, $\dot{\phi} = 10\ s^{-1}$. Nital is used as etching agent.

700 °C is observed, see Fig. 6b and 6d. The difference in grain size depending on the annealing temperature is attributed to faster grain growth at higher temperatures.

With increasing strain, the tendency for recrystallization increases. Fig. 7 shows the resulting microstructure for the experiment with $T_S = 600$ °C at the lateral position in the longitudinal plane at R_{eff} of the specimen, see Fig. 2, with a measured temperature at the surface of 576 °C (thermocouple position edge, as schematized in Fig. 2). A temperature gradient and heat transfer towards the gripping area explain the decreased temperature at the edge position compared to the center position.

The bigger diameter in the gripping area of the sample leads to supporting effects of the near gripping regions of the gauge area and thus decreases the degree of deformation. The shear strain γ_{acc} increases in the longitudinal plane towards the center (from left to right in Fig. 7) of the specimen. With Eq. (3), measured inclination angles of 62° and 65° indicate accumulated shear strains γ_{acc} of 1.80 and 2.15, respectively.

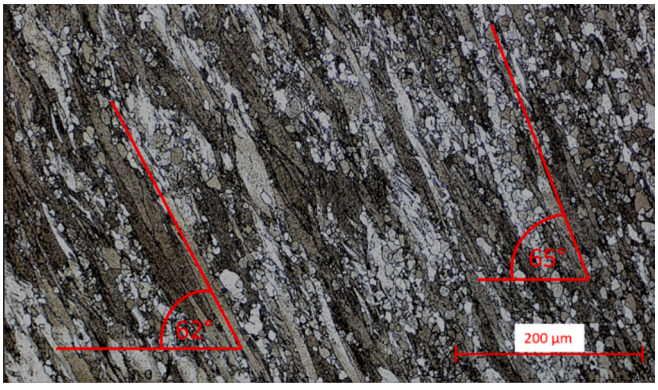

Fig. 7. Edge position in the longitudinal plane at R_{eff} with measured $T_{surface} = 576$ °C and $\dot{\phi} = 10\ s^{-1}$. The degree of deformation increases from left to right simultaneously with the recrystallized fraction.

We observe an increase of the recrystallized grain fraction towards the sample center in the longitudinal plane with increasing γ_{acc}. In Fig. 7, it is notable that the nucleation of recrystallized grains predominantly occurs at grain boundaries, which is the favored nucleation site for static recrystallization according to Humphreys and Hatherley [2].

Investigating the cross-section plane of the samples provides insight into the recrystallization kinetics and the grain size evolution in dependence of strain across the radius. Fig. 8 shows the resulting microstructure in the cross-section in radial direction from the sample center to the edge after torsional deformation and annealing at 600 °C.

Following Eq. (1), the resulting strain increases with the radius, which directly influences the recrystallization behavior and grain size. Three markings indicate the regions with: a) only slight deformation and without recrystallization, (b) with more deformation and some recrystallization, and (c) with full recrystallization, respectively. With increasing strain across the radius, the recrystallized fraction increases, and the resulting grain size decreases. Fig. 9 shows the evolution of the microstructure over the radius in more detail, with respect to Fig. 8. With increasing strain across the radius, from a to c in Fig. 8, the recrystallized fraction increases, and the average grain size decreases. With increasing recrystallized fraction, we observe that the fraction of highly deformed areas decreases, indicating a decrease in dislocation density in the already recrystallized areas [2]. This is corroborated by the EBSD measurement mappings in Figs. 10 and 11.

5.2. EBSD analysis

We use EBSD to investigate the interrelation of the recrystallization behavior of the material with the misorientation, following an approach by Wright et al. [19], in dependence on the applied strain. Fig. 10 shows the result of an EBSD mapping in the cross-section at radius $R = 0.54$ mm ($\varepsilon_{eff} = 0.28$) of the sample annealed at 600 °C after deformation. In Fig. 10, the mappings of inverse pole figure (IPF), image quality (IQ), kernel average misorientation (KAM), and GND-density are given. IPF, IQ, and KAM give insight into the local deformation condition of a microstructure. Uniform coloring inside a grain in the inverse pole figure

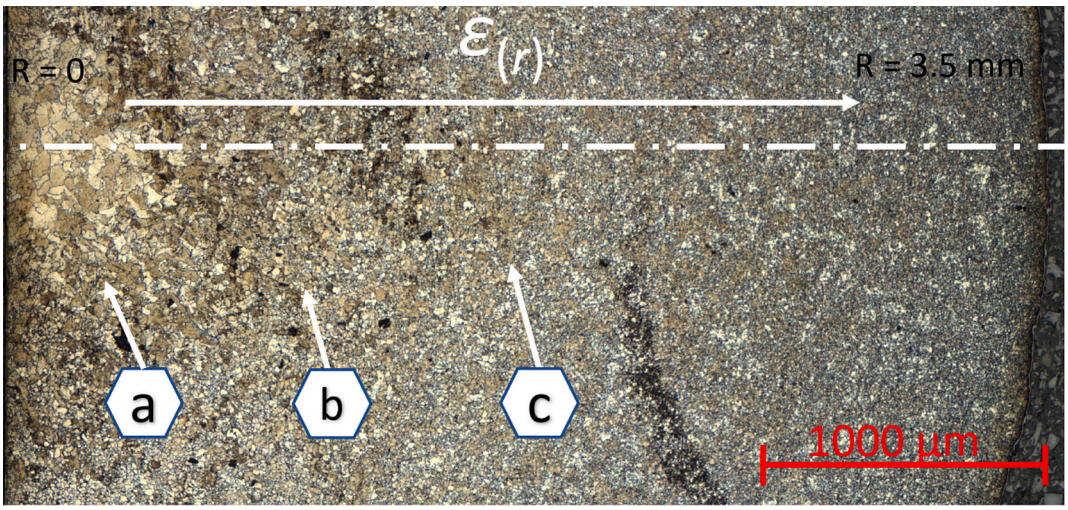

Fig. 8. Cross-section after torsion test as described in section 2.1 and annealing at 600 °C for 120 s, the dash-dotted line is the radial connection from the sample center to the edge. The evolution of the resulting microstructure is directly influenced by the resulting strain across the radius. For insight into positions a, b, and c, see Fig. 9.

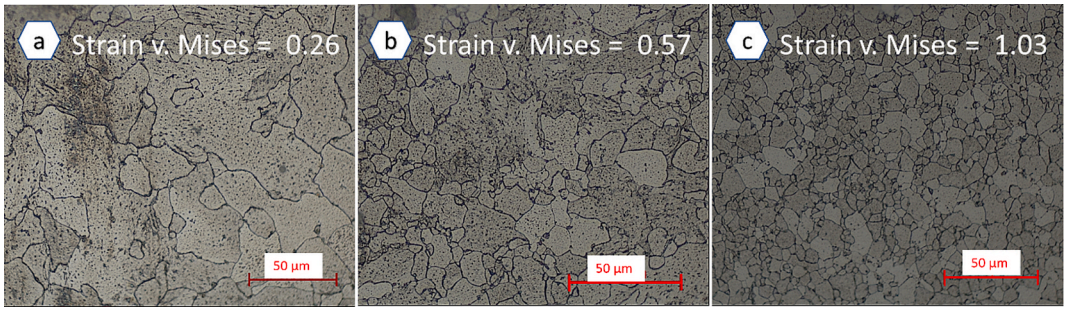

Fig. 9. Cross-section, detail of Fig. 8 with part a) referring to the low-deformed and hardly recrystallized center part ($\varepsilon_{eff} = 0.26$). Part b) intermediate area with deformed grains and some small recrystallized grains ($\varepsilon_{eff} = 0.57$), and part c) fully recrystallized site in the cross-section ($\varepsilon_{eff} = 1.03$).

map without deviation in the color tone suggests homogeneous orientation and no or only shallow deformation. Brighter areas in the IQ mapping show better pattern quality and indicate a low misorientation value, provided that the sample preparation across the sample surface is homogeneous. Blue and red lines in the IQ map indicate LAGBs and HAGBs, respectively. KAM gives the local misorientation of a pixel concerning its vicinity. It should be noted that only directly connected neighbors (1st order) from the same grain are considered for calculating the KAM. White areas show no misorientation and indicate regions of freshly recrystallized microstructure. With image analysis, we measure the white areas and are thus able to evaluate the recrystallized fraction.

Fig. 10d shows the calculated GND-density using the approach of Pantleon [20], see Section 2.4.2. The darker and recrystallized grains indicate areas with a lower dislocation density, i.e., GND-density close to equilibrium dislocation density of about 10^{12} m^{-2}. The brighter and not recrystallized areas give a GND-density of $5 \cdot 10^{14}$ m^{-2} corresponding to an increase of more than two orders of magnitude compared to the already recrystallized grains. The dislocation density in the non-recrystallized areas for a strain of 0.28 varies from $2 \cdot 10^{14}$ m^{-2} to $8 \cdot 10^{14}$ m^{-2}. This high deformation level and resulting high dislocation density provide the driving pressure for recrystallization, following the Bailey-Hirsch mechanism [33].

Fig. 11 shows KAM mappings in the cross-section for the sample annealed at 600 °C across the radius from 0.1 mm to 1.24 mm and effective strain ε_{eff} from 0.05 to 0.65. HAGBs are marked with continuous black lines. The recrystallization behavior clearly varies across the radius and resulting strain. With increasing strain, the fraction of recrystallized volume (white areas) increases, and the resulting grain size decreases. The misorientation in the KAM mappings increases with increasing strain and turns zero after recrystallization.

As mentioned in Section 2.4, areas with low KAM value (white areas) and no misorientation within the grain can be assumed to be fully recrystallized. The radius position at 0.24 mm ($\varepsilon_{eff} = 0.13$) corresponds to the recrystallization limit. The mapping is indicative of the fact that grain boundaries are the preferred nucleation site for recrystallized grains [2].

The contents of the trace elements in the material, like sulfur, copper, chromium, and aluminum (see Table 1), are small and in a typical range for industrially used steel. Although these elements at these low fractions have an influence on the boundary mobility, their influence is not any further considered. Instead, we assume a boundary mobility typically for technologically pure steel.

5.3. Evaluated grain sizes and recrystallized fractions

The grain size and recrystallized fraction versus the effective strain ε_{eff} are evaluated in the cross-section plane depending on the radius position via Eq. (2). Fig. 12 depicts the grain size (dashed lines and triangles) and the recrystallized fraction (continuous lines and circles) after torsion test and annealing for 120 s at 600 °C (filled symbols) and 700 °C (empty symbols), respectively. The average grain size quickly decreases with increasing strain till it reaches a saturation level, which strongly depends on the soaking temperature [2]. After reaching a particular degree of deformation, increasing the deformation at

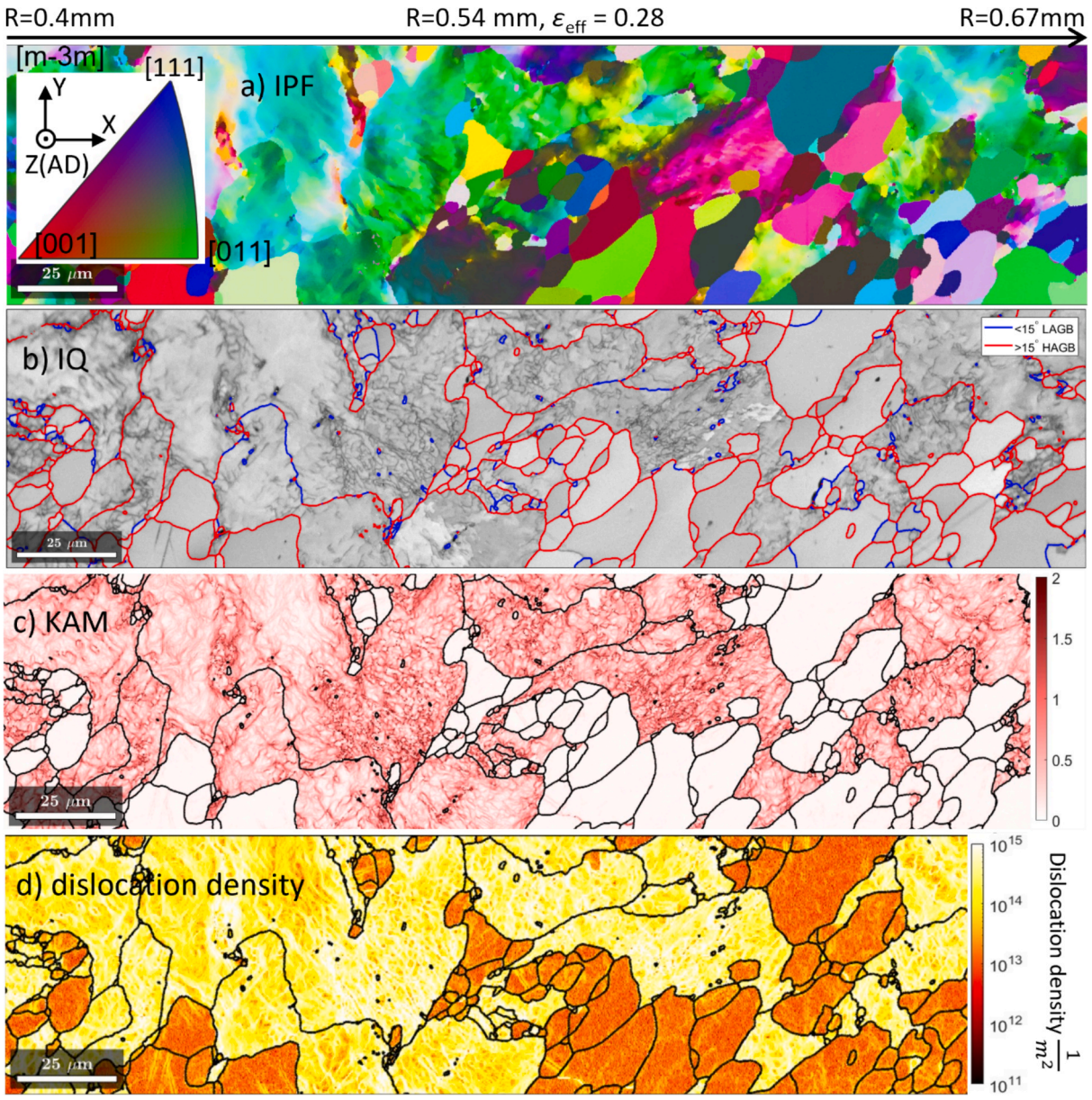

Fig. 10. EBSD-mapping of the cross-section of the sample annealed at 600 °C after deformation at position R = 0.54 mm (ε_{eff} = 0.28). a) IPF in reference with the axial direction (AD), giving insight into the orientations within the microstructure, b) IQ with HAGB and LAGB and c) KAM, used to measure the recrystallized fraction. d) GND-density, according to Pantleon [20].

approximately 0.8 strain does not further decrease the ferrite grain size. Regarding the recrystallized fraction, we see that the microstructure at 700 °C is already fully recrystallized at a much lower strain. This is due to the increase of grain boundary mobility with increasing temperature, thus facilitating the recrystallization mechanism at higher temperatures.

The grain size is represented in the graph with error bars indicating the standard error of the mean. The substantial error bars observed in the low strain data can be attributed to incomplete recrystallization occurring at low strain levels. At low strain, a bimodal distribution of the grain size is evident, with recrystallized grains exhibiting a significant decrease in grain size, as illustrated in the KAM − mapping in Fig. 11.

6. Simulation results and discussion

MatCalc [37], a toolbox for thermokinetic simulation, is used to simulate the recrystallization behavior and grain size evolution in dependence on strain and temperature. The thermodynamic basis for the thermokinetic simulation provides the Calphad-developed [70], open-source database mc_fe.tdb [71]. The models implemented and used in MatCalc [37] for the substructure evolution, recrystallization, and grain growth are presented in Section 3. The model for the substructure evolution is parameterized using a measured flow curve.

6.1. Phase stabilities

The thermodynamic equilibrium phase stabilities in the studied alloy RFE80 as a function of temperature are shown in Fig. 13. The ferrite to austenite phase boundary is at 720 °C. Aluminum nitride (AlN), MnS, and cementite (Fe_3C) are present in equilibrium. Following the equilibrium simulation in Fig. 13, we do not expect phase transformations in the experimental temperature range up to 700 °C.

Lückl et al. [73] investigate the co-precipitation of AlN and MnS in low-carbon steel and find AlN nucleation facilitated at MnS. The authors [73] state that precipitates of MnS and AlN at grain boundaries and AlN

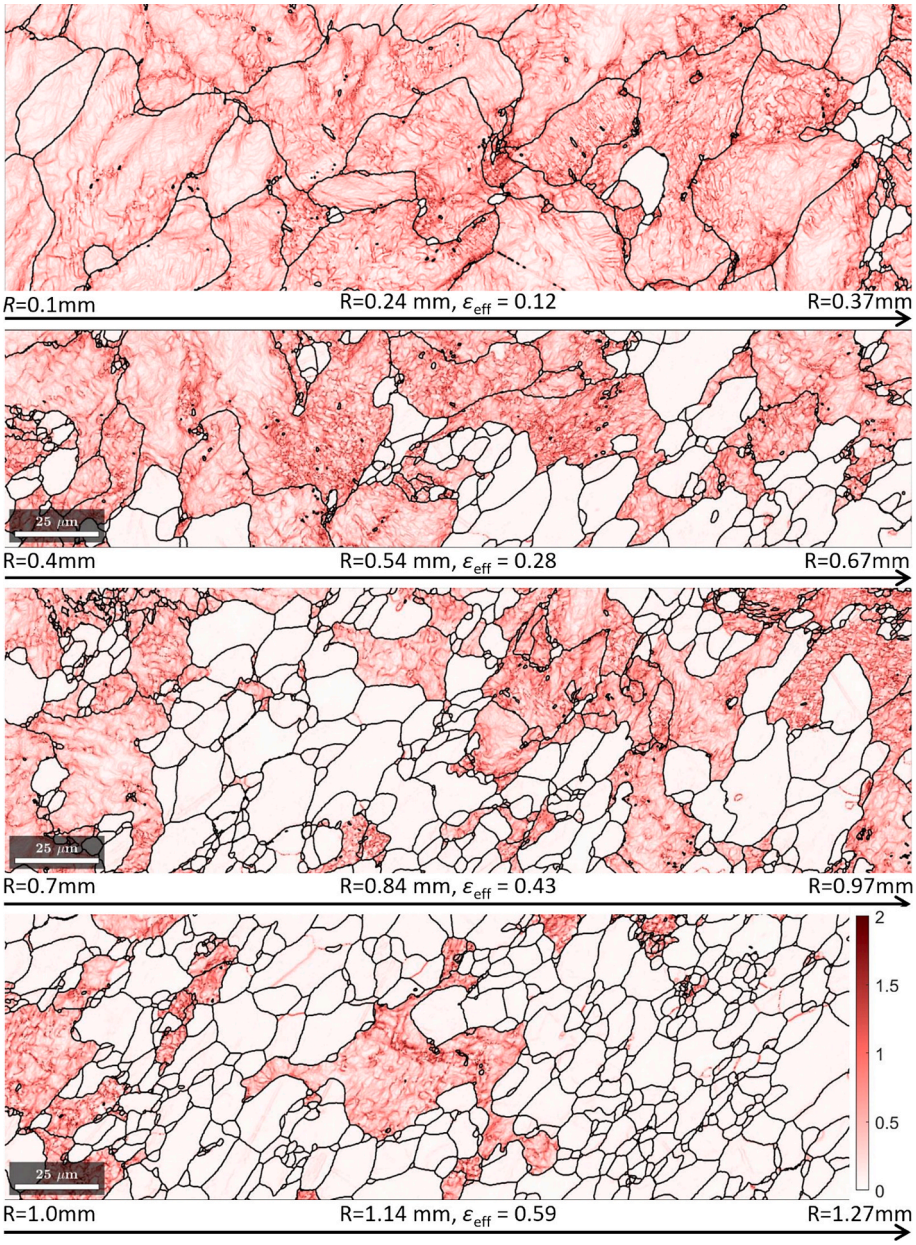

Fig. 11. KAM mapping after EBSD-measurement of the cross-section of the sample annealed at 600 °C for the radius position ranging from 0.1 mm to 1.27 mm (corresponding ε_{eff} = 0.05–0.65). The white areas with low KAM and no misorientation within the grain are recrystallized. Note that the recrystallization behavior clearly varies across the radius.

on primary MnS are, on average, some hundred nanometers large, which is too large to provide any notable Zener-drag [74]. Regarding the experimentally applied annealing temperatures in the range up to 700 °C, we conclude from the constant phase stabilities in this temperature range and the results of Lückl et al. [73] (i.e., considering the AlN and MnS precipitate size) that precipitates do not play a role for the recrystallization and grain growth behavior of this alloy.

6.2. Simulated flow curve and dislocation density evolution

To parameterize the strengthening coefficients A, B, C, and Θ_{AV} (see Table 3) of the dislocation density evolution model, we use a measured flow curve of the RFE80 material, dotted line in Fig. 14, from a compression test at 200 °C with a strain rate of 10 s^{-1}. The flow curve of the RFE80 material, which is used for parametrization, is evaluated via a compression test on a Gleeble thermomechanical simulator [41]. To accurately address the actual material behavior in the Gleeble compression test [75], it is necessary to take into account the stiffness of the thermomechanical simulator and a temperature correction assuming the peak of the temperature evolution at the end of the deformation segment. The influence of friction between the specimen and the components of the thermomechanical simulator is disregarded for strain values up to 0.8. To ensure the reliability of the experimental results, the experiments are repeated. The v. Mises criterion [46] is applied to compare the results from torsional deformation with simulation results.

In Fig. 14, we see a slight reduction of the experimental flow curve at a strain of 0.3, which shows a clear deviation from the ideal shape of the flow curve, as described by Kocks and Mecking [38]. These authors [38] state the correlation of the Taylor Equation (Eq. (14)) holds for all cases where the flow stress is purely controlled by dislocation–dislocation interaction. In the case of bcc-structures, at lower temperatures deviations can be observed [38]. It is reported that the formation of cleared

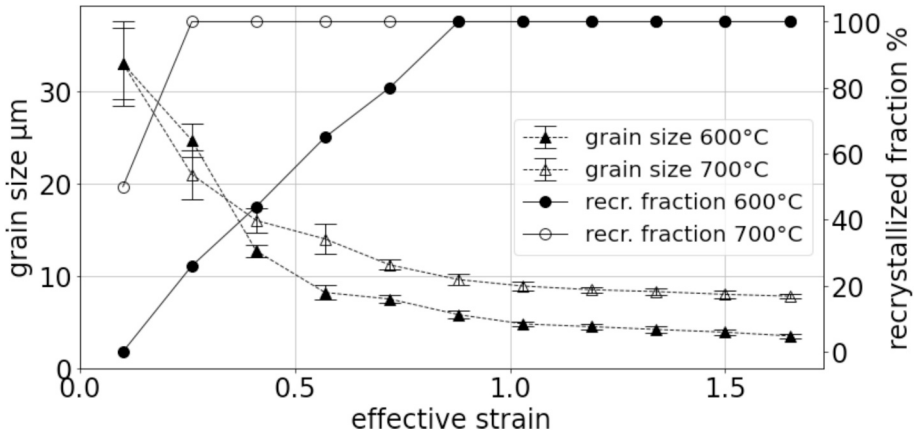

Fig. 12. Experimentally evaluated grain size (dashed line) and recrystallized fraction (continuous line) after torsion test and annealing for 120 s at 600 °C (filled markers) and 700 °C (empty markers), respectively. The grain size is represented graphically with error bars, which correspond to the standard error of the mean.

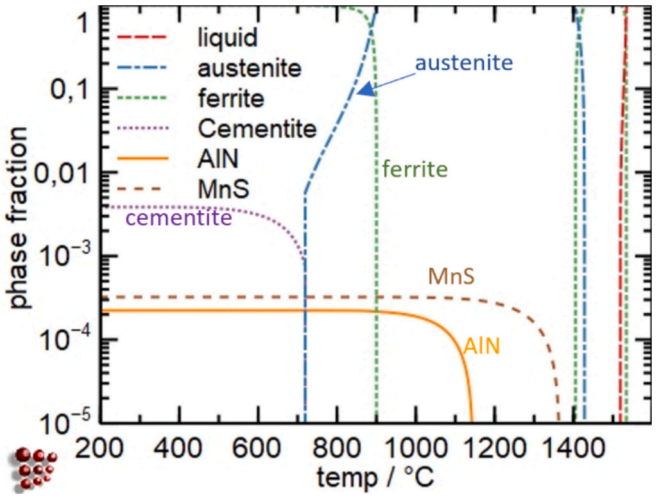

Fig. 13. Stepped equilibrium calculation; Phase fraction over the temperature in °C of the used steel RFE80; Used thermodynamic database: mc_fe.tdb [72].

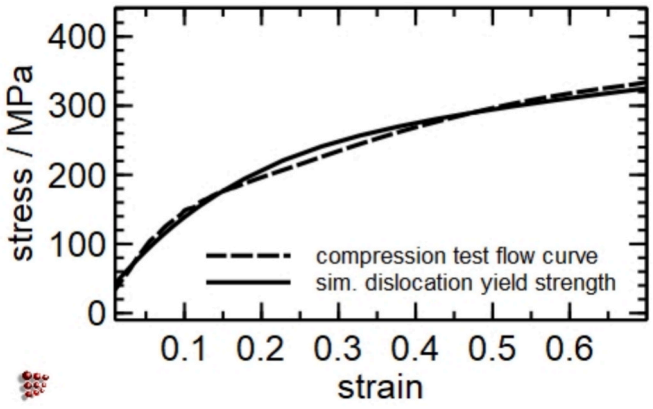

Fig. 14. Measured flow curve (200 °C, 10 s^{-1}) from compression test (dashed line) and simulation result (continuous line) with calibrated parameters *A*, *B*, *C*, *and* Θ_{AV} from Table 3.

slip channels is the reason for this behavior at low temperatures in bcc-structures [76], resulting in an anisotropic dislocation density evolution [77]. In any case, the simplified model for the substructure evolution from Section 3.1 still shows good agreement with the behavior of the real material.

For correctly describing the evolution of the wall dislocation density and the resulting total dislocation density, see Section 3.1, an appropriate description of the evolution of the subgrain boundary misorientation Θ_{AV} over strain is needed to accurately predict the slope of the linear part of the flow curve (stage IV hardening [38]). In turn, the total dislocation density directly influences the driving pressure for recrystallization, so correctly describing Θ_{AV} is crucial (see Eq. (6)). Using a cubic root function for Θ_{AV} provides reasonable misorientation values, especially for low strains up to $\varepsilon_{eff} = 1$.

Fig. 15 compares the simulated dislocation density evolution, using the parameters from Table 3, with the experimental dislocation density evolution data from Despujols et al. [78] and Tanaka et al. [79] at different strains for low-carbon steel.

The measurement error of the dislocation density has been documented to be substantial in the extant literature [79,80]. Following this, this type of comparison in Fig. 15 indicates that the amount of deformation energy being stored within the material, representing the driving force for SRX, is in the correct order of magnitude [33]. The present experimentally derived GND-density, see Fig. 10, of approximately $5 \cdot 10^{14}$ m^{-2} also agrees with the simulated dislocation density evolution, marked as a star in Fig. 15. The binding energy for the solute drag contribution of Mn is taken as 1000 $Jmol^{-1}$, which agrees well with the literature data [6,7].

6.3. Simulated recrystallized fraction and grain size

The fraction of statically recrystallized microstructure (Fig. 16) and the grain growth behavior (Fig. 17) are simulated for the thermo-mechanical treatment of Fig. 1. Fig. 16 compares the recrystallized fraction from the simulation (continuous lines) and the experimental values (dashed lines) with respect to the effective strain after von Mises (compare to Eq. (2) and [46]).

The static recrystallization behavior is compared for 600 °C (triangles) and 700 °C (circles) soaking temperatures. A good agreement between simulation and experiment is obtained using the parametrization from Table 3.

In Fig. 17, the experimentally measured grain size evolution (dashed lines) is compared to the simulation (continuous lines) versus the effective strain for 600 °C (triangles) and 700 °C (circles) soaking temperatures.

The grain size simulation at 600 °C overestimates the measured grain sizes up to a strain of 0.7. At 700 °C, the grain size simulation underestimates the measured value until reaching a strain of 0.8. The correct description of the mobility of grain boundaries and the interaction between solute and grain boundary is highly complex and widely

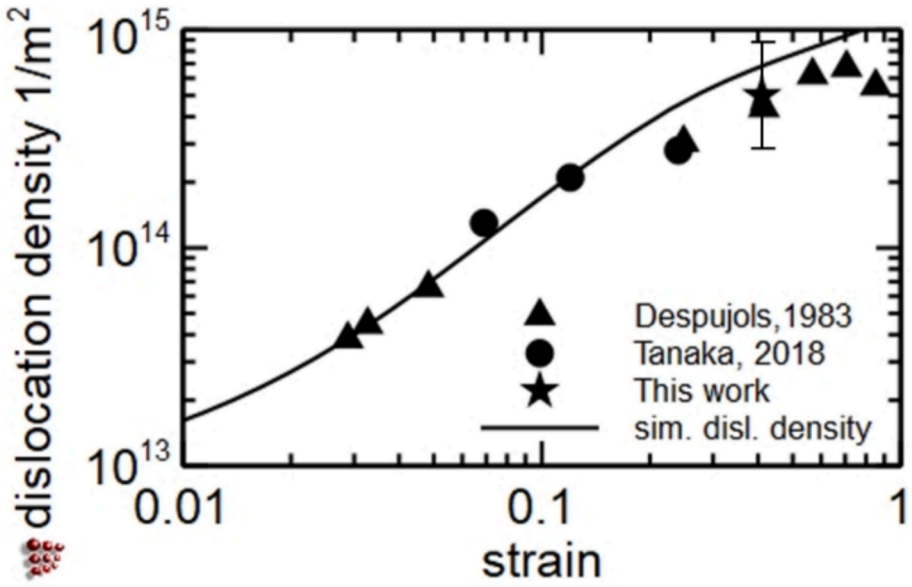

Fig. 15. Simulated dislocation density evolution (continuous line) as a function of strain in comparison to experimental data [78,79]. The experimentaly measured GND-density, see Fig. 10, is marked as star with error bar.

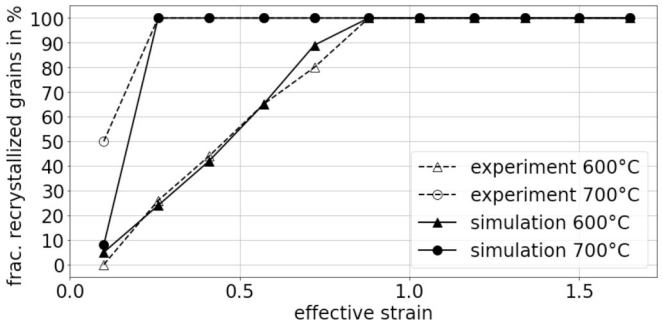

Fig. 16. Evolution of the recrystallized fraction as a function of effective strain using the von Mises criterion [26]. Comparison of experiment (dashed lines) and simulation (continuous lines) for torsion testing at room temperature and subsequent annealing for 120 s at 600 °C (triangles) and 700 °C (circles), respectively.

dependent on temperature [81], type of solute, and solute concentration [6,7]. We see good agreement in the saturation level of the grain size, with data points lying within the experimental error bar. A promising trend in the low-strain region is seen, suggesting that the applied approach captures the key aspects of the underlying physics.

The simulations are primarily influenced by the dislocation density, which serves as the driving force for recrystallization. Another important factor pertains to the mobility of grain boundaries. In general, grain boundary mobility is particularly influenced by intrinsic mobility and retardation forces resulting from solute drag and Zener pinning. It is noteworthy that the low alloying element fraction in the studied alloy serves to minimize the influence on grain boundary mobility, with Mn proving to be the primary effective element. The dislocation density evolution is evaluated by employing a mean-field approach, wherein the accurate description of the subgrain boundary misorientation evolution is imperative to precisely describe the behavior of the flow curve during stage IV hardening. In essence, this approach considers only one type of glide system without explicit consideration of edge and screw dislocation characteristics and a constant Burgers vector. On one hand, these simplifications affect the accuracy of the simulation. On the other hand,

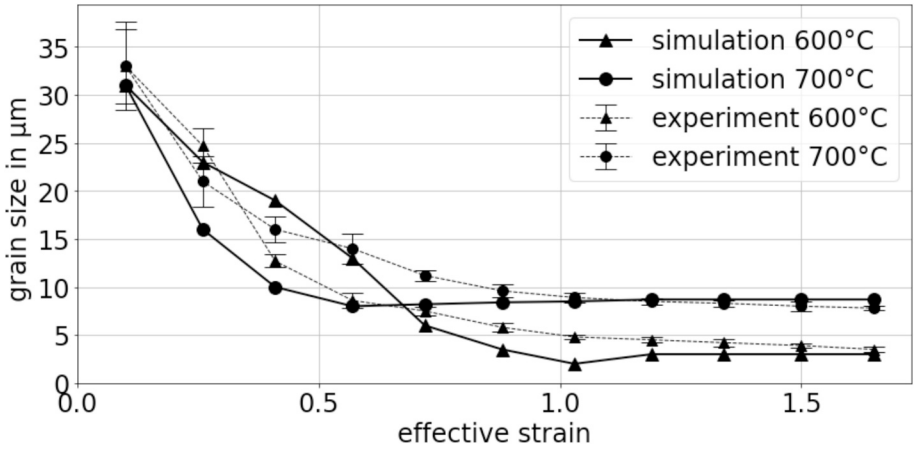

Fig. 17. Grain size evolution over effective strain using the von Mises criterion [26]. Comparison of experiment (dashed lines) and simulation (continuous lines) for torsion testing at room temperature and subsequent annealing for 120 s at 600 °C (triangles) and 700 °C (circles), respectively. The experimental result of the grain size is represented graphically with error bars, which correspond to the standard error of the mean. Lines are a guide to the eye.

the mean-field approach enables fast-forward simulations, a low number of calibration parameters, and the applicability for multi-component systems with precipitation and solute drag [37,82]. Trustfull validation of the dislocation density evolution is given by comparison of the yield strength (see Fig. 14) via the Taylor equation (Eq. 14) and with experimental dislocation density values (see Fig. 15). No definitive approach for determining precise error bars is available regarding the accuracy of the simulation setup. Furthermore, systematic model errors resulting from imperfect modeling cannot be quantified as statistical model errors [83,84]. Consequently, validation of model outcomes with experimental results is imperative.

7. Conclusions

Torsion tests provide a convenient possibility to investigate high strain levels and significant strain variations with only a few experiments in low-carbon steels. The experimental results show a decrease of the recrystallized grain size with increasing strain before reaching a saturation level. The annealing temperature influences the grain size at the saturation level.

The SRX simulations agree well with the experimental data regarding the recrystallized grain size after deformation and subsequent annealing when the subgrain boundary misorientation is considered in the modeling, using a cubic root function for its description.

The ABC parameters of the extended mean-field Kocks-Mecking model for the dislocation density evolution are calibrated with a suitable flow-curve, allowing for the simulation of the dislocation density evolution in agreement with GND-density data evaluated from EBSD experiments. To correctly picture the behavior during stage IV hardening, a cubic root function for the subgrain boundary misorientation is developed.

The correct description of the grain boundary mobility is confirmed by the consistency between simulative and experimental results, revealing decreasing grain size with increasing strain until a saturation level is reached at an effective strain of roughly one. The annealing temperature strongly influences the level of saturation of the resulting grain size. The strain rate during the cold deformation process does not measurably influence the resulting microstructure in the present work.

The predictive power of the present SRX simulations for ultra-low carbon steel helps to reduce the number of prior experimental investigations within industrial processes.

CRediT authorship contribution statement

Markus Führer: Writing – original draft, Visualization, Validation, Software, Methodology, Investigation, Conceptualization. **Philipp Retzl:** Writing – review & editing, Software. **Robert Kahlenberg:** Writing – review & editing, Software. **Sabine Zamberger:** Writing – review & editing. **Phillip Haslberger:** Writing – review & editing, Conceptualization. **Ernst Kozeschnik:** Writing – review & editing, Software. **Erwin Povoden-Karadeniz:** Writing – review & editing, Supervision, Conceptualization.

Funding

This research was funded by Christian Doppler Forschungsgesellschaft in the framework of the CD-Laboratory of Interfaces and Precipitation Engineering (CDL-IPE).

Declaration of competing interest

The authors declare that they have no known competing financial interests or personal relationships that could have appeared to influence the work reported in this paper.

Acknowledgments

The financial support from the Austrian Federal Ministry for Digital and Economic Affairs and the National Foundation for Research, Technology, and Development is gratefully acknowledged. The authors acknowledge Open Access Funding by TU Wien. The financial support, as well as the provision of sample material by voestalpine Forschungsservicegesellschaft, is gratefully acknowledged by the authors.

Data availability

Data will be made available on request.

References

[1] J. Unglaub, Dissertation: Einfluss von Eigenspannungen auf die Ermüdungsfestigkeit Großer Schrauben, Technischen Universität Carolo-Wilhelmina, Braunschweig, 2018.
[2] F.J. Humphreys, M. Hatherly, Recrystallization and Related Annealing Phenomena, Elsevier Science, 2004.
[3] M. Scheffler, W.D. Callister, D.G. Rethwisch, (Eds.). Materialwissenschaften Und Werkstofftechnik. Eine Einführung, 1. Auflage, 2020, Wiley-VCH GmbH, Weinheim.
[4] M. Diehl, L. Kertsch, K. Traka, et al., Site-specific quasi in situ investigation of primary static recrystallization in a low carbon steel, Mater. Sci. Eng. A 755 (2019) 295–306, https://doi.org/10.1016/j.msea.2019.02.032.
[5] Z. Nasiri, S. Ghaemifar, M. Naghizadeh, et al., Thermal mechanisms of grain refinement in steels: a review, Met. Mater. Int. 27 (7) (2021) 2078–2094, https://doi.org/10.1007/s12540-020-00700-1.
[6] H.S. Zurob, D. Panahi, C.R. Hutchinson, et al., Self-consistent model for planar ferrite growth in Fe-C-X Alloys, Metall. Mater. Trans. A 44 (8) (2013) 3456–3471, https://doi.org/10.1007/s11661-012-1479-8.
[7] I.-E. Benrabah, H.P. van Landeghem, F. Bonnet, et al., Solute drag modeling for ferrite growth kinetics during precipitation experiments, Acta Mater. 221 (2021) 117364, https://doi.org/10.1016/j.actamat.2021.117364.
[8] E. Sobotka, J. Kreyca, R. Kahlenberg, et al., Analysis of recrystallization kinetics concerning the experimental, computational, and empirical evaluation of critical temperatures for static recrystallization in Nb, Ti, and V microalloyed steels, Metals 13 (5) (2023) 884, https://doi.org/10.3390/met13050884.
[9] S. Vervynckt, K. Verbeken, B. Lopez, et al., Modern HSLA steels and role of non-recrystallisation temperature, Int. Mater. Rev. 57 (4) (2013) 187–207, https://doi.org/10.1179/1743280411y.0000000013.
[10] M. Gómez, L. Rancel, S.F. Medina, Effects of aluminium and nitrogen on static recrystallisation in V-microalloyed steels, Mater. Sci. Eng. A 506 (1–2) (2009) 165–173, https://doi.org/10.1016/j.msea.2008.11.049.
[11] S.F. Medina, Determination of no-recrystallisation temperature in Nb-V-Ti microalloyed steel and discussion of its definition, Mater. Sci. Technol. 14 (3) (1998) 217–221, https://doi.org/10.1179/mst.1998.14.3.217.
[12] T. Ogawa, N. Maruyama, N. Sugiura, et al., Incomplete recrystallization and subsequent microstructural evolution during intercritical annealing in cold-rolled low carbon steels, ISIJ Int. 50 (3) (2010) 469–475, https://doi.org/10.2355/isijinternational.50.469.
[13] C. Herrera, N.B. Lima, A.F. Filho, et al., Texture and mechanical properties evolution of a deep drawing medium carbon steel during cold rolling and subsequent recrystallization, J. Mater. Process. Technol. 209 (7) (2009) 3518–3524, https://doi.org/10.1016/j.jmatprotec.2008.08.007.
[14] M. Tavakoli, H. Mirzadeh, M. Zamani, Ferrite recrystallisation and intercritical annealing of cold-rolled low alloy medium carbon steel, Mater. Res. Express 35 (16) (2019) 1932–1941, https://doi.org/10.1080/02670836.2019.1655862.
[15] M. Tavakoli, H. Mirzadeh, M. Zamani, Static recrystallization kinetics of ferrite in cold-deformed medium carbon steel, Mater. Res. Express 6 (12) (2019) 1265g9, https://doi.org/10.1088/2053-1591/ab6895.
[16] A. Chbihi, D. Barbier, L. Germain, et al., Interactions between ferrite recrystallization and austenite formation in high-strength steels, J Mater Sci 49 (10) (2014) 3608–3621, https://doi.org/10.1007/s10853-014-8029-2.
[17] K.K. Alaneme, Influence of tempered microstructures on the transformation behaviour of cold deformed and intercritically annealed medium carbon low alloy steel, Mat. Res. 13 (2) (2010) 203–209, https://doi.org/10.1590/S1516-14392010000200014.
[18] B.M. Whitley, A.L. Araujo, J.G. Speer, et al., Analysis of microstructure in hot torsion simulation, Mater. Perform. Charact. 4 (3) (2015), https://doi.org/10.1520/mpc20150012. MPC20150012.
[19] S.I. Wright, M.M. Nowell, D.P. Field, A review of strain analysis using electron backscatter diffraction, Microscopy Microanal. 17 (3) (2011) 316–329, https://doi.org/10.1017/S1431927611000055.
[20] W. Pantleon, Resolving the geometrically necessary dislocation content by conventional electron backscattering diffraction, Scr. Mater. 58 (11) (2008) 994–997, https://doi.org/10.1016/j.scriptamat.2008.01.050.
[21] J. Nye, Some geometrical relations in dislocated crystals, Acta Metall. 1 (2) (1953) 153–162, https://doi.org/10.1016/0001-6160(53)90054-6.

[22] M.F. Ashby, The deformation of plastically non-homogeneous materials, Philos. Magazine: J. Theoretical Exp. Appl. Phys. 21 (170) (1970) 399–424, https://doi.org/10.1080/14786437008238426.

[23] A. Arsenlis, D. Parks, Crystallographic aspects of geometrically-necessary and statistically-stored dislocation density, Acta Mater. 47 (5) (1999) 1597–1611, https://doi.org/10.1016/S1359-6454(99)00020-8.

[24] E. Breitbarth, S. Zaefferer, F. Archie, et al., Evolution of Dislocation Patterns inside the Plastic Zone Introduced by Fatigue in an Aged Aluminium Alloy AA2024-T3., 09215093 718, 2018, 345–349, 10.1016/j.msea.2018.01.068.

[25] C. Zhu, T. Harrington, G.T. Gray, et al. Dislocation-Type Evolution in Quasi-Statically Compressed Polycrystalline Nickel, 13596454, 155, 2018, 104–116, 10.1016/j.actamat.2018.05.022.

[26] G.I. Taylor, The mechanism of plastic deformation of crystals. Part I.—Theoretical, Proc. R. Soc. Lond. A 145 (855) (1934) 362–387, https://doi.org/10.1098/rspa.1934.0106.

[27] C.W. Price, Use of Kolmogorov-Johnson-Mehl-Avrami kinetics in recrystallization of metals and crystallization of metallic glasses, Acta Metall. Mater. 38 (5) (1990) 727–738, https://doi.org/10.1016/0956-7151(90)90024-B.

[28] P.R. Rios, E. Villa, Transformation kinetics for inhomogeneous nucleation, Acta Mater. 57 (4) (2009) 1199–1208, https://doi.org/10.1016/j.actamat.2008.11.003.

[29] S.F. Medina, A. Quispe, Improved model for static recrystallization kinetics of hot deformed austenite in low alloy and Nb/V microalloyed steels, ISIJ Int. 41 (7) (2001) 774–781, https://doi.org/10.2355/isijinternational.41.774.

[30] M. Avrami, Kinetics of phase change. II Transformation-time relations for random distribution of nuclei, J. Chem. Phys. 8 (2) (1940) 212–224, https://doi.org/10.1063/1.1750631.

[31] M.K. Rehman, H.S. Zurob, A novel approach to model static recrystallization of austenite during hot rolling of Nb microalloyed steel. Part I: precipitate-free case, Metall. Mater. Trans. A 44 (4) (2013) 1862–1871, https://doi.org/10.1007/s11661-012-1526-5.

[32] J.W. Cahn, The impurity-drag effect in grain boundary motion, Acta Metall. 10 (9) (1962) 789–798, https://doi.org/10.1016/0001-6160(62)90092-5.

[33] J.E. Bailey, P.M. Hirsch, The recrystallization process in some polycrystalline metals, Proc. R. Soc. Lond. A 267 (1328) (1962) 11–30, https://doi.org/10.1098/rspa.1962.0080.

[34] J. Gil Sevillano, P. van Houtte, E. Aernoudt, Large strain work hardening and textures, Prog. Mater Sci. 25 (2–4) (1980) 69–134, https://doi.org/10.1016/0079-6425(80)90001-8.

[35] R. Kaibyshev, K. Shipilova, F. Musin, et al., Continuous dynamic recrystallization in an Al–Li–Mg–Sc alloy during equal-channel angular extrusion, Mater. Sci. Eng. A 396 (1–2) (2005) 341–351, https://doi.org/10.1016/j.msea.2005.01.053.

[36] E. Nes. Modelling of work hardening and stress saturation in FCC Metals. 00796425 41(3): 129–193, 1997. doi: 10.1016/s0079-6425(97)00032-7.

[37] E. Kozeschnik. Mean-Field Microstructure Kinetics Modeling(In: Francisca G. Caballero (ed.), Encyclopedia of Materials: Metals and Alloys. vol. 4,): 521–526, 2022. doi: 10.1016/b978-0-12-819726-4.00055-7.

[38] U.F. Kocks, H. Mecking, Physics and phenomenology of strain hardening: the FCC case, Prog. Mater Sci. 48 (3) (2003) 171–273, https://doi.org/10.1016/S0079-6425(02)00003-8.

[39] H. Buken, E. Kozeschnik, A model for static recrystallization with simultaneous precipitation and solute drag, Metall. Mater. Trans. A 48 (6) (2017) 2812–2818, https://doi.org/10.1007/s11661-016-3524-5.

[40] J. Calvo, L. Collins, S. Yue, Design of microalloyed steel hot rolling schedules by torsion testing: average schedule vs real schedule, ISIJ Int. 50 (8) (2010) 1193–1199, https://doi.org/10.2355/isijinternational.50.1193.

[41] Gleeble (2023) thermomechanical Simulator. https://www.gleeble.com/. Accessed 20 Jul 2023.

[42] P.A. Manohar, M. Ferry, T. Chandra, Five decades of the Zener Equation, ISIJ Int. 38 (9) (1998) 913–924, https://doi.org/10.2355/isijinternational.38.913.

[43] E. Gdoutos, M. Konsta-Gdoutos, Compression, bending, torsion and multiaxial testing, Mech. Test. Mater. 275 (2024) 35–61, https://doi.org/10.1007/978-3-031-45990-0_2.

[44] K.P. Rao, E.B. Hawbolt, H.J. McQueen, et al., Constitutive relationships for hot deformation of a carbon steel: a comparison study of compression tests and torsion tests, 0008-4433, 32(2), 1993, 165–175, 10.1179/cmq.1993.32.2.165.

[45] A. Gräber, K. Pöhlandt, State of the art of the torsion test for determining flow curves. Steel Res. 61(5): 212–218, 10.1002/srin.199000334.

[46] T.M. Maccagno, J.J. Jonas, S. Yue, et al., Determination of recrystallization stop temperature from rolling mill logs and comparison with laboratory simulation results, ISIJ Int. 34 (11) (1994) 917–922, https://doi.org/10.2355/isijinternational.34.917.

[47] W.H.J. Barraclough, K.D. Nair, et al., Effect of specimen geometry on hot torsion test results for solid and tubular specimens, J. Test. Eval. 1 (3) (1973) 220–226, https://doi.org/10.1520/JTE10007J.

[48] D.A. Hughes, N. Hansen. High angle boundaries formed by grain subdivision mechanisms. 13596454 45(9), 1997: 3871–3886. doi: 10.1016/S1359-6454(97)00027-X.

[49] (2024) Metallic grain structures and microscopic analysis insight | Struers.com. https://www.struers.com/en/Knowledge/Materials/Metallic-grain-structures#. Accessed 06 Jun 2024.

[50] R. Hielscher, H. Schaeben, A novel pole figure inversion method: specification of the MTEX algorithm, J. Appl. Cryst. 41 (6) (2008) 1024–1037, https://doi.org/10.1107/S0021889808030112.

[51] E. Macherauch, H.-W. Zoch. Korngrößenermittlung. In: Praktikum in Werkstoffkunde. Vieweg+Teubner, 2011, pp. 75–81.

[52] H. Buken, E. Kozeschnik, A model for static recrystallization with simultaneous precipitation and solute drag, Metall. Mater. Trans. A 48 (6) (2021) 2812–2818, https://doi.org/10.1007/s11661-016-3524-5.

[53] E. Kozeschnik, Modeling Solid-State Precipitation, Momentum Press, New York, NY, 2013.

[54] U.F. Kocks, H. Mecking, Physics and Phenomenology of Strain Hardening: The FCC Case. 00796425 48(3): (1993) 171–273. doi: 10.1016/s0079-6425(02)00003-8.

[55] P. Sherstnev, P. Lang, E. Kozeschnik. Treatment of Simultaneous Deformation and Solid-State Precipitation in Thermo-Kinetic Calculations. CD-ROM Proceedings of the 6th European Congress on Computational Methods in Applied Sciences and Engineering (ECCOMAS 2012), September 10-14, 2012, Vienna, Austria, 2012: 8.

[56] G. Stechauner, E. Kozeschnik, Self-diffusion in grain boundaries and dislocation pipes in Al, Fe, and Ni and application to AlN precipitation in steel, Mater. Eng. Performance 23 (5) (2014) 1576–1579, https://doi.org/10.1007/s11665-014-0921-z.

[57] W.T. Read, W. Shockley, Dislocation models of crystal grain boundaries, American Physical Society 78 (3) (1950) 275, https://doi.org/10.1103/PhysRev.78.275.

[58] T. Sakai, A. Belyakov, H. Miura, Ultrafine grain formation in ferritic stainless steel during severe plastic deformation, Metall. Mater. Trans. A 39 (9) (2008) 2206–2214, https://doi.org/10.1007/s11661-008-9556-8.

[59] T. Sakai, A. Belyakov, R. Kaibyshev, et al., Dynamic and post-dynamic recrystallization under hot, cold and severe plastic deformation conditions, Prog. Mater Sci. 60 (2014) 130–207, https://doi.org/10.1016/j.pmatsci.2013.09.002.

[60] K. Tsuzaki, X. Huang, T. Maki, Mechanism of dynamic continuous recrystallization during superplastic deformation in a microduplex stainless steel, Acta Mater. 44 (11) (1996) 4491–4499, https://doi.org/10.1016/1359-6454(96)00080-8.

[61] K. Huang, R.E. Logé, A review of dynamic recrystallization phenomena in metallic materials, Mater. Des. 111 (2016) 548–574, https://doi.org/10.1016/j.matdes.2016.09.012.

[62] F. Schuh, M. von Heimendahl, (1987). Z. Metallkunde 65(346).

[63] M.R. Staker, D.L. Holt, The dislocation cell size and dislocation density in copper deformed at temperatures between 25 and 700°C. 00016160 20(4): 569–579. doi: 10.1016/0001-6160(72)90012-0.

[64] H. Buken, S. Zamberger, E. Kozeschnik. A model for the influence of micro-alloying elements on static recrystallization of austenite. Proceedings of the 6th International Conference on Recrystallization and Grain Growth (ReX&GG 2016): 113–118, 2016.

[65] H. Mughrabi, The alpha-factor in the Taylor flow-stress law in monotonic, cyclic and quasi-stationary deformations: dependence on slip mode, dislocation arrangement and density, Curr. Opin. Solid State Mater. Sci. 20 (6) (2016) 411–420, https://doi.org/10.1016/j.cossms.2016.07.001.

[66] E. Sobotka, J. Kreyca, M.C. Poletti, et al., Analysis and modeling of stress-strain curves in microalloyed steels based on a dislocation density evolution model, Materials 15 (19) (2022) 6824, https://doi.org/10.3390/ma15196824.

[67] G. Stechauner, E. Kozeschnik, Assessment of substitutional self-diffusion along short-circuit paths in Al, Fe and Ni, Calphad 47 (2014) 92–99, https://doi.org/10.1016/j.calphad.2014.06.008.

[68] R. Ueji, N. Tsuji, Y. Minamino, et al., Effect of rolling reduction on ultrafine grained structure and mechanical properties of low-carbon steel thermomechanically processed from martensite starting structure, Sci. Technol. Adv. Mater. 5 (1–2) (2004) 153–162, https://doi.org/10.1016/j.stam.2003.10.017.

[69] D. Raabe, 23 - Recovery and recrystallization: phenomena, physics, models, simulation, in: D.E. Laughlin, K. Hono (Eds.), Physical Metallurgy, 5th ed., Elsevier Science, Burlington, 2014, pp. 2291–2397.

[70] L. Kaufman, H. Bernstein, Computer Calculation of Phase Diagrams. With Special Reference to Refractory Metals, Academic Press Inc, New York, 1970.

[71] (2024) Matcalc – Solid State and Kinetics Precipitation. https://www.matcalc.at/index.php/databases/open-databases. Accessed 29 Jul 2024.

[72] Matcalc – Solid State and Kinetics Precipitation. https://www.matcalc.at/. https://www.matcalc.at/. Accessed 11 Aug 2023.

[73] M. Lückl, T. Wojcik, E. Povoden-Karadeniz, et al., Co-precipitation behavior of MnS and AlN in a low-carbon steel, Steel Res. 89 (3) (2018) 1700342, https://doi.org/10.1002/srin.201700342.

[74] C. Zener, Grains, phase, and Interfaces : an interpretation of microstructure, Trans. Am. Inst. Min. Metall. Soc. 175 (1948) 15.

[75] C.J. Bennett, S.B. Leen, E.J. Williams, et al., A critical analysis of plastic flow behaviour in axisymmetric isothermal and Gleeble compression testing, Comput. Mater. Sci 50 (1) (2010) 125–137, https://doi.org/10.1016/j.commatsci.2010.07.016.

[76] B. Brenner, A. Luft, The mechanism of work softening in cold-worked molybdenum polycrystals at an elevated temperature. 0025-5416 52(3): 229–237. doi: 10.1016/0025-5416(82)90150-1.

[77] E.I. Galindo-Nava, P. Rivera-Díaz-del-Castillo, Modelling plastic deformation in BCC metals: dynamic recovery and cell formation effects, Mater. Sci. Eng. A 558 (2012) 641–648, https://doi.org/10.1016/j.msea.2012.08.068.

[78] B. Amiot, J. Despujols, Strains in extra-low-carbon steel sheets after weak (skin-pass) rolling, Mater. Sci. Technol. 10 (1) (1983) 161–166, https://doi.org/10.1179/030716983803291532.

[79] Y. Tanaka, S. Takaki, T. Tsuchiyama, et al., Effect of GRAIN SIZE ON THE YIELD STRESS OF COLD WORKED IRon, ISIJ Int. 58 (10) (2018) 1927–1933, https://doi.org/10.2355/isijinternational.ISIJINT-2018-371.

[80] C. Moussa, M. Bernacki, R. Besnard, et al., Statistical analysis of dislocations and dislocation boundaries from EBSD data, Ultramicroscopy 179 (2017) 63–72, https://doi.org/10.1016/j.ultramic.2017.04.005.

[81] U.F. Kocks, Solute drag as an upper bound to high-temperature strength11Dedicated to John Price Hirth and Johannes Weertman, Scr. Mater. 39 (4–5) (1998) 431–436, https://doi.org/10.1016/S1359-6462(98)00218-8.
[82] P. Retzl, Y.V. Shan, E. Sobotka, et al., Progress of Physics-based Mean-field Modeling and Simulation of Steel, BHM Berg- Und Hüttenmännische Monatshefte 167 (1) (2022) 15–22, https://doi.org/10.1007/s00501-021-01188-x.
[83] J. Dobaczewski, W. Nazarewicz, P.-G. Reinhard, Error estimates of theoretical models: a guide, J. Phys. G: Nucl. Part. Phys. 41 (7) (2014) 74001, https://doi.org/10.1088/0954-3899/41/7/074001.
[84] A. Tarantola, Inverse Problem Theory and Methods for Model Parameter Estimation, Society for Industrial and Applied Mathematics, 2005.